

CONFERENCES AND SYMPOSIA

PACS numbers: 42.82.Cr, 52.25.Os, **52.59. – f**, **52.70. – m**, **52.77. – j**

Plasma-based sources of extreme ultraviolet radiation for lithography and mask inspection

(50th anniversary of the Institute of Spectroscopy, Russian Academy of Sciences)

D B Abramenko, P S Antsiferov, D I Astakhov, A Yu Vinokhodov, I Yu Vichev, R R Gayazov, A S Grushin, L A Dorokhin, V V Ivanov, D A Kim, K N Koshelev, P V Krainov, M S Krivokorytov, V M Krivtsun, B V Lakatosh, A A Lash, V V Medvedev, A N Ryabtsev, Yu V Sidelnikov, E P Snegirev, A D Solomyannaya, M V Spiridonov, I P Tsygvintsev, O F Yakushev, A A Yakushkin

DOI: https://doi.org/10.3367/UFNe.2018.06.038447

Contents

Abstract. We report on the development of plasma-based sources of extreme ultraviolet radiation for the next-generation lithography and mask inspection and the development of equipment for spectral diagnostics of such sources.

D B Abramenko [1,2], **P S Antsiferov** [1], **D I Astakhov** [1,3], **A Yu Vinokhodov** [2], **I Yu Vichev** [4], **R R Gayazov** [1], **A S Grushin** [4], **L A Dorokhin** [1], **V V Ivanov** [1,2], **D A Kim** [4], **K N Koshelev** [1,2], **P V Krainov** [5], **M S Krivokorytov** [1,2,5], **V M Krivtsun** [1,2,5], **B V Lakatosh** [5], **A A Lash** [2], **V V Medvedev** [1,3,5], **A N Ryabtsev** [1], **Yu V Sidelnikov** [1], **E P Snegirev** [1], **A D Solomyannaya** [4], **M V Spiridonov** [6,2], **I P Tsygvintsev** [4], **O F Yakushev** [7], **A A Yakushkin** [2]

[1] Institute of Spectroscopy, Russian Academy of Sciences, ul. Fizicheskaya 5, 108840 Troitsk, Moscow, Russian Federation

[2] EUV Labs, Ltd., ul. Promyshlennaya 2B, 108841 Troitsk, Moscow, Russian Federation

[3] ISTEQ B.V., High Tech Campus 9, 5656 AE Eindhoven, Netherlands

[4] Keldysh Institute of Applied Mathematics, Russian Academy of Sciences, Miusskaya pl. 4, 125047 Moscow, Russian Federation

[5] Moscow Institute of Physics and Technology (State University), Institutskii per. 9, 141700 Dolgoprudnyi, Moscow region, Russian Federation

[6] Prokhorov General Physics Institute, Russian Academy of Sciences, ul. Vavilova 38, 119991 Moscow, Russian Federation

[7] Lebedev Physical Institute, Russian Academy of Sciences, Leninskii prosp. 53, 119991 Moscow, Russian Federation

E-mail: medvedev@phystech.edu

Received 28 August 2018

Uspekhi Fizicheskikh Nauk **189** (3) 323 – 334 (2019)

DOI: https://doi.org/10.3367/UFNr.2018.06.038447

Translated by E N Ragozin; edited by A M Semikhatov

Keywords: EUV lithography, laser-produced plasma, radiation sources

1. Introduction

Projection photolithography (or simply lithography) is one of the key technological processes in the modern microelectronics industry. Lithography is used for the layer-by-layer production of an integrated circuit (IC) on the surface of a silicon chip coated with a photosensitive material (photoresist). For this, a quasimonochromatic radiation source is used to illuminate a photomask that carries the image of a certain layer of the IC under production. The projection of this image is transferred with strong demagnification on the surface of the silicon wafer, where the photoresist exposure takes place. The past 50 years have seen unprecedented development of microelectronics, provided by the continual reduction in the characteristic size of IC elements. This was made possible largely due to improvements in lithography technologies.

The minimal size of the elements produced in optical imaging is limited below by diffraction effects. According to the Rayleigh criterion, the smallest lateral size of the elements in the image plane is

$$L_{\min} = \frac{k\lambda}{\mathrm{NA}}\,, \tag{1}$$

where λ is the wavelength of the radiation in use, NA is the numerical aperture of the optical projection system, and k is the proportionality coefficient. A reduction in $L_{\min}$ is

achieved, for instance, by increasing NA (immersion lithography), effectively decreasing k (for instance, by the multiple exposure process), or shortening the wavelength λ. For several decades, $L_{\min}$ was reduced by shortening the wavelength of the radiation sources used in lithography technologies.

In the 1980s, mercury lamps ($\lambda = 365$ nm) served as the main lithography source. In the early 1990s, they were replaced by KrF excimer lasers, which operate in the deep ultraviolet (UV) region ($\lambda = 248$ nm). Presently, ArF excimer lasers, which generate $\lambda = 193$ nm radiation, are the main lithography tool. The next step on the path of wavelength reduction is to pass to extreme ultraviolet (EUV) radiation with a wavelength $\lambda \sim 10$ nm [1]. EUV lithography is aimed at the production of ICs with a minimal characteristic element size less than 10 nm.

The transition of lithography to the EUV region has required the mastering and industrialization of new or, to be more precise, unusual ways of radiation generation for the semiconductor industry. The use of EUV lithography for the mass production of microcircuits requires an average radiation power of at least 20 W [2], which can be provided only by plasma radiation sources and free-electron lasers. Free-electron lasers require huge capital investments: such facilities become profitable for an average output power above 1 kW [3]. At present, the main thrust is directed towards the development and improvement of high-power plasma sources of EUV radiation [4–6].

Early in the development of plasma radiation sources, the question arose about the working substance [7–10]. Comprehensive investigations suggested that the plasma of multiply charged tin (Sn) ions showed the greatest promise [10–12]. The ions $Sn^{8+}-Sn^{13+}$ have $4d^k-(4d^{k-1}4f+4p^54d^{k+1})$ resonance transitions, which give rise to high-intensity EUV tin plasma radiation with $\lambda \sim 10$ nm. As shown in Refs [11, 12], the strong 4d–4f exchange interaction in the $4d^{k-1}4f$ configuration and the strong 4p–4d exchange interaction in the $4p^54d^{k+1}$ configuration are responsible for the separation of the energy levels of these configurations into two bands, the transition probabilities from the upper band being much greater than those from the lower band. The strong interaction of the $4d^{k-1}4f$ and $4p^54d^{k+1}$ configurations leads to an even greater narrowing of this radiation band. As a result, despite the existence of many hundreds of levels in a broad energy range, the radiation is concentrated in a relatively narrow spectral range about $\lambda = 13.5$ nm (Fig. 1). It is noteworthy that the lithographic process involves the radiation in a narrow spectral range of 13.5 ± 0.135 nm, which is defined by the effective transmission band of the optical lithographic system [13].

There are two main approaches to the construction of high-power tin-plasma radiation sources [14, 15]. The first involves the use of a vacuum-spark pulsed electric discharge [16–18]. The second approach is to harness the plasma produced in ablation of the material by high-power laser pulses [4, 6]. In both cases, one of the most important source characteristics is the conversion efficiency (CE), the ratio of the radiative energy in the 13.5 ± 0.135 nm range emanating into a solid angle of 2π sr in the direction of the collector mirror to the energy delivered to the plasma (Fig. 2, which shows a diagram of a laser plasma EUV radiation source). Experimental investigations of different configurations of tin vapor discharges have shown that the highest CE for such discharges is about 3% [18]. Laser plasma allows reaching a

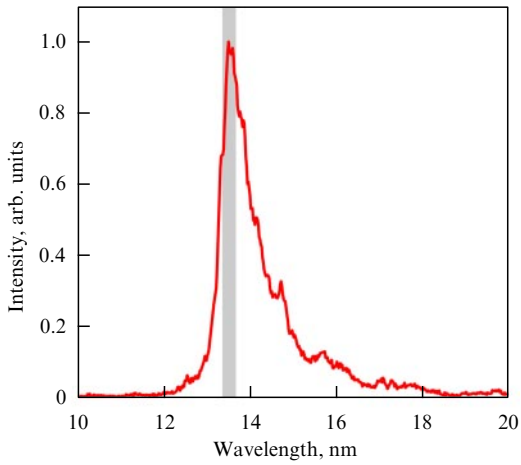

Figure 1. Emission spectrum of the tin plasma produced by irradiating a planar target by pulses of a transversely excited (TEA) CO_2 laser. The vertical grey band shows the spectral range $\lambda = 13.5 \pm 0.135$ nm.

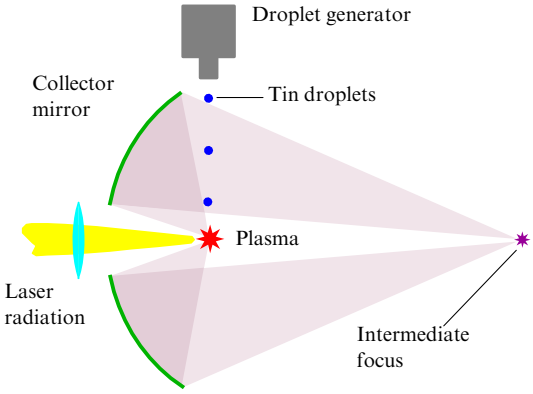

Figure 2. Diagram of a laser plasma EUV radiation source.

CE in the range of 6–7% [19]. Apart from its higher CE, laser plasma also offers other advantages in comparison with discharge plasmas. First, in laser plasma sources, the role of targets can be played by tin microspheres. The use of these targets of limited mass permits the contamination rate of the first mirror (collector) to be significantly moderated, which is one of the most acute problems that face the designers of industrial EUV lithographic facilities. Second, laser plasma permits the use of normal-incidence optics, which entails an increase in the angle of useful radiation collection. The combination of the above advantages impelled the industry to decide in favor of laser plasma sources.

Apart from the demand for high-power radiation sources for EUV lithography, there is a demand for low-power EUV radiation sources that nevertheless have a high brightness. These sources are needed for inspecting the contamination of a lithographic mask by nano- and microparticles. This technological process is termed actinic inspection. Actinic inspection requires a radiation source with a wavelength $\lambda = 13.5$ nm and an energy brightness of at least 100 W mm^{-2} sr^{-1} [20].

In the early 2000s, the Institute for Spectroscopy of the Russian Academy of Sciences (ISAN) joined the International Academic Consortium concerned with EUV lithography problems and proposed the idea of using tin plasmas to

design high-power EUV radiation sources [10]. In this paper, we describe the contribution of the institute in collaboration with other research groups (Keldysh Institute of Applied Mathematics of the RAS (KIAM RAS), Lebedev Physical Institute (LPI), RAS, and Skobeltsyn Institute of Nuclear Physics (SINP) of Lomonosov Moscow State University) in solving research problems related to the development of high-power radiation sources for lithography. Also covered are ISAN achievements in the development of high-brightness EUV radiation sources and equipment intended for the spectral diagnostics of EUV radiation sources.

2. High-power extreme ultraviolet radiation source

The laser-plasma source of EUV radiation is illustrated in Fig. 2. The flow of droplet targets in the source is produced with a droplet generator, whose operation is based on the principle of induced jet disintegration [21]. Droplet targets several dozen micrometers in diameter are sequentially irradiated by two laser pulses. The first, the prepulse, fulfils the function of optimizing the target shape by a relatively weak ablative action. The spherical droplet undergoes a strong variation of its shape and fragmentation under prepulse irradiation. The second pulse, the main one, transforms the target material into the plasma state by ablation. The intensity of the main laser pulse is selected such that the plasma is heated to a temperature of several tens of electron-volts to produce Sn^{8+}–Sn^{13+} ions, which radiate near $\lambda = 13.5$ nm. The resultant plasma is at the focus of an elliptic collector mirror, which collects the radiation and relays it to the second focus of the ellipse, the so-called intermediate focus. The radiation is next relayed from the intermediate focus to the optical lithography system, which irradiates the photomask and transfers its highly demagnified image to the surface of the silicon wafer under exposure.

2.1 Optimal plasma properties

Successful operation of such a complex setup as an EUV radiation source is hardly possible without numerical simulations. Specifically, improving the conversion efficiency requires the use of radiative hydrodynamics (RHD) codes to simulate the main source operation phase — the ablation of the target material by the main laser pulse with the subsequent heating of the resultant plasma and the reradiation of the input energy in the EUV range. Carrying out these simulations requires knowing the radiative and thermodynamic properties of tin plasma in the absence of thermodynamic equilibrium. For this, a version of the THERMOS code [22, 23] based on the collisional-radiative equilibrium model was developed at the KIAM RAS [24]. The simulations use the Reduced Detailed Configuration Accounting (RDCA) atomic database [25] constructed using the average atom model, with the spectral line positions and oscillator strengths refined using the RCG [26] and FAC [27] detailed codes. The spectral data were additionally refined and compared with the measurements on a high-resolution grazing-incidence spectrometer [28]. The rate coefficients for collisional processes were calculated by the Lotz [29–32] and Regemorter [33] approximate formulas. The Kramers approximation [34] was employed to calculate the photoionization rate. The autoionization rate and dielectronic recombination rate coefficients were calculated in the dipole approximation [35].

As a rule, RHD codes use tables based on either equilibrium (LTE) or transparent (coronal) plasma [36], which does not furnish an adequate picture of the processes occurring in the experimental plasma. Under these conditions, the energy transfer is effected by radiation, and the inclusion of the radiation field therefore determines the net result of simulations, in particular, the charge state composition of the plasma for a given temperature and density, which in turn determines the spectral radiation distribution generated by the source and its efficiency. It was suggested that the nonequilibrium radiation field between two limit cases — optically thin and optically thick plasmas — be interpolated using the generalized escape factor [37]

$$\xi = \frac{\int F_{\rm rad}\,\mathrm{d}S}{4\pi \int\int j^1(\omega)\,\mathrm{d}\omega\,\mathrm{d}V}\,,$$

where $F_{\rm rad}$ is the radiation flux, S is the surface area of some characteristic volume V (for instance, a spatial cell or layer), ω is the photon energy, and $j^1(\omega)$ is the emissivity corresponding to the case of optically thick plasma.

Then, in solving the radiation transfer equation, the opacity and emissivity can be used in the forms [38, 39]

$$k(\omega) = \xi k^1(\omega) + (1-\xi)\,k^0(\omega)\,,$$

$$j(\omega) = \xi j^1(\omega) + (1-\xi)\,j^0(\omega)\,,$$

where k^0, k^1 and j^0, j^1 — the absorption coefficients and the emissivities — are borrowed from tables pre-calculated under the corresponding approximations. Here, the superscript '0' corresponds to the transparent case and '1' to the optically thick one. Because the parameter ξ depends on the solution of the radiation transfer equation, several iterations are required to obtain ξ consistent with the actual radiation field. The table is calculated under the approximation of an optically transparent plasma, i.e., with the radiation field $U_0(\omega) = 0$. In the second limit case of an optically thick plasma, the relation $U_1(\omega) = U_L(\omega)$ is used for the radiation field of a planar plasma layer of a given thickness L.

Apart from direct use in RHD simulations, the thus obtained tables of radiative and thermodynamic properties permit making several preliminary estimates. We consider the spectral purity (SP), which is defined as the ratio of the plasma emissivity in the spectral band $\delta\lambda = 13.5 \pm 0.135$ nm to the total emissivity:

$$\mathrm{SP} = \frac{\int_{13.365}^{13.635} j^1(\lambda)\,\mathrm{d}\lambda}{\int_0^{+\infty} j^1(\lambda)\,\mathrm{d}\lambda} \times 100\%\,,$$

where λ is the wavelengths in nm. Spectral purity is used for quantitative estimates of the production efficiency of EUV radiation of the required wavelength.

The spectral radiation purity for tin plasmas is plotted as a function of the temperature and density in Fig. 3. An analysis of this dependence shows that there is an $(N_{\rm i}, T_{\rm e})$-parameter domain in which the requisite spectral band accounts for more than 40% of the total radiant energy of the plasma. This domain is enclosed by a black curve in Fig. 3. As can be assumed, producing an efficient EUV radiation source requires generating a plasma with parameters lying within this domain: the temperature must be in the range $T_{\rm e} = 20-90$ eV and the ion density must be of the order of $N_{\rm i} \sim 10^{17}-10^{19}$ cm^{-3}. It is at these parameters that the

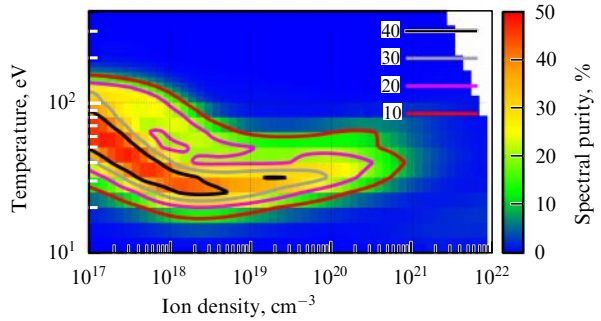

Figure 3. Spectral radiation purity SP as a function of the temperature and ion density in the case of optically thick plasma with the U_L radiation field for $L = 300$ μm.

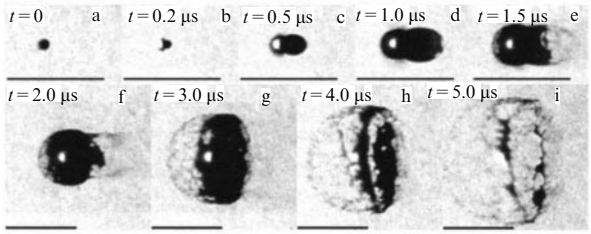

Figure 4. Shadow photographs of a liquid metal droplet (material: eutectic In–Sn alloy; diameter: 56 μm) (a) prior to and (b–i) after its irradiation by a titanium:sapphire laser pulse. The laser radiation propagates from left to right in the plane of the drawing. The pulse duration is 0.8 ps (full width at half maximum). The average intensity on the surface of the droplet target is 7×10^{13} W cm^{-2}. The scale lengths in the pictures correspond to 500 μm. © American Physical Society. Reproduced with permission.

$Sn^{+8} - Sn^{+13}$ ions, which make the main contribution to the $13.5 \pm 1\%$ nm radiation band, are present in sufficient numbers. Lower-density domains, despite a rather high spectral purity, make a small contribution to the total radiation power, because the emissivity scales as $j \propto N_i^3$. That is, generating the requisite radiation flux for a low plasma density would require a significant increase in the geometric plasma size, which is impossible due to the limitations imposed by the optical subsystem of the facility. In the higher-density domain, the short-wavelength radiation is largely reabsorbed by the plasma and does not make an appreciable contribution to the EUV source efficiency.

2.2 Optimization of target shape

Experiments with the first prototypes of industrial EUV radiation sources with tin microdroplet targets showed that the highest laser-to-EUV radiation energy conversion coefficient did not exceed 1% [4]. Based on experimental and theoretical investigations [40], it was found that one of the main reasons for the low conversion coefficient is a low percentage of absorbed laser energy, not higher than 20%: the low effective area of the droplet targets and high density gradients have the effect that the greater part of the laser energy is either reflected or scattered. Furthermore, as suggested by theoretical estimates, tin plasma with the ion density $N_i \sim 10^{17} - 10^{19}$ cm^{-3} is optimal for $\lambda = 13.5$ nm radiation. The density of tin atoms in a droplet corresponds to the condensed matter state: $N_i \sim 10^{23}$ cm^{-3}. Evidently, this difference between the initial material density and the optimal plasma density is also a kind of obstruction, which has to be overcome in the course of laser ablation of the target. To improve the energy input efficiency for the main laser pulse and produce a plasma with optimal characteristics for EUV radiation, it was proposed to change the spatial configuration of the target (droplet) with the use of a laser prepulse.

We assume that the initial tin droplet undergoes fragmentation under some external action, to turn into a cloud of droplets of significantly smaller size ($\sim 0.1 - 1$ μm), and this debris cloud expands. In this case, a significant increase occurs in the effective target surface area compared with the area of the initial spherical droplet. As a consequence, in the irradiation of this target by the main laser pulse, the fraction of absorbed laser energy and the material ablation rate are much higher. The plasma then occupies the volume encompassing the debris cloud. In this case, the spatial debris density directly affects the plasma density. The target modified this way allows reaching the optimal plasma density and temperature much faster. Furthermore, by varying the prepulse parameters, it is possible to control the spatial plasma distribution, which is required for optimizing the radiation absorption of the main laser pulse.

The main purpose of the laser prepulse is precisely to optimize the target. For instance, the fragmentation of tin droplets can be effected by femtosecond or picosecond laser pulses. Experimental research on the disintegration of liquid metallic droplets under irradiation by chirped pulses of a titanium:sapphire laser was carried out at the ISAN [41–45]. Figure 4 shows the droplet shape evolution under irradiation by a picosecond pulse with the average intensity $I \approx 7 \times 10^{13}$ W cm^{-2}. Each image in Fig. 4 is an instantaneous shadow photograph obtained some time after the arrival of the titanium:sapphire laser pulse. We can see that the droplet initially undergoes a large expansion, turning into a complex structure consisting of two cavities surrounded by a liquid metal shell. As a result, a cloud of fragments concentrated in a structure reminiscent of a dome or a hemisphere in shape is produced. As suggested by numerical simulations, this picture of droplet disintegration is caused by the passage of a shock wave produced by the ablative action of very short laser pulses [45, 46].

Pulses $\tau_L \sim 10$ ns in duration were regarded as an alternative to a short picosecond prepulse [47–49]. Experimental investigations of the ablative action of Nd:YAG laser pulses on liquid metal targets were also carried out at the ISAN. The shape evolution of a droplet irradiated by an Nd:YAG laser pulse with the average intensity $I \approx 5 \times 10^9$ W cm^{-2} on the target surface is exemplified in Fig. 5. It can be seen that the droplet undergoes a strong deformation and turns into a thin metallic disk. This target also permits a significant increase in the ablation rate and the percentage of absorbed energy of the main laser pulse in comparison with the initial droplet target.

2.3 Production of EUV-radiating plasma

The main pulse ablates the target material and transforms this material into a plasma with parameters that permit an efficient generation of useful EUV radiation. As noted above, the optimal plasma parameters for the production of EUV radiation are $T_e = 20 - 90$ eV and $N_i \approx 3 \times 10^{18}$ cm^{-3}.

Modern laser technologies allow producing high-power CO_2 gas lasers with a wavelength of 10.6 μm and solid-state Nd:YAG lasers with a wavelength of 1.064 μm (a variety of lasers can be made, but only these two are left in view of the

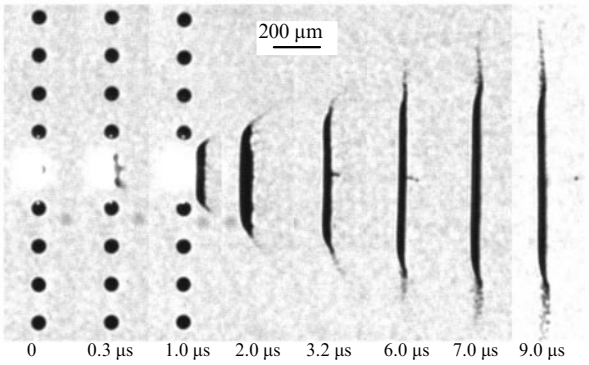

Figure 5. Shadow photographs of a liquid metal droplet (material: eutectic In–Sn alloy; diameter: 70 μm) prior to and after irradiation by an Nd:YAG laser pulse. The laser radiation propagates from left to right in the plane of the drawing. The pulse duration is 18 ns (full width at half maximum). The average intensity on the surface of the droplet target is to 5×10^9 W cm^{-2}.

requirement of a high repetition rate). The choice between these two versions is determined by the basic aspects of laser radiation–matter interaction. Infrared radiation interacts primarily with the electron gas of the plasma. Laser radiation propagates from a vacuum towards dense plasma layers. In this case, the radiation does not penetrate the layers with the electron densities higher than the critical density

$$N_e^c \approx \frac{10^{21}}{\lambda_L^3}\,, \qquad (2)$$

where N_e^c is measured in cm^{-3} and the laser wavelength λ_L in μm. In plasma configurations typical for the EUV source, the greater part of laser radiation is absorbed in precisely the layers with a density close to N_e^c. For the Nd:YAG laser, the critical electron density is equal to 10^{21} cm^{-3} and for the CO_2 laser, to 10^{19} cm^{-3}. Therefore, the CO_2 laser radiation is absorbed in plasma layers whose density is close to the plasma density optimal for the generation of useful EUV radiation. The Nd:YAG laser radiation is absorbed in the plasma layers of a much higher density, which correspond to a lower spectral purity of the output radiation and a lower conversion efficiency of laser radiation to the plasma radiation in the working spectral band $\delta\lambda = 13.5 \pm 0.135$ nm. Experimental investigations performed by different research groups showed that the use of Nd:YAG lasers permits reaching the efficiency of conversion to useful radiation CE = 2.0–2.5% [50], while the use of a CO_2 laser allows obtaining CE = 6–7% [19]. Considering these qualitative and quantitative arguments, the designers of industrial EUV radiation sources decided to give preference to CO_2 lasers.

Developing an efficient EUV radiation source requires a detailed study of the interaction of the main laser pulse with the target. Various processes show up in the interaction of high-power laser radiation with a substance: target material ablation, laser radiation absorption in the vapor of this material and in the plasma, ionization and recombination, as well as the emission and absorption of short-wavelength radiation in the plasma, and eventually the plasma expansion. Experimentally, it is relatively easy to measure several integral characteristics of laser plasma, like the emission spectrum, the size of the region radiating in a certain spectral range, and the ion kinetic energy spectrum. However, these data do not permit the above physical processes to be characterized completely, which complicates the search for basic options for optimizing the EUV source operation. This generates the need for a theoretical simulation of the laser-driven source. For this, an RHD code RZLINE was developed at the ISAN, which allows simulating the physical processes occurring in plasma short-wavelength radiation sources. The RZLINE code is described elsewhere [51]. It was validated by comparing the data of numerical simulations with the experimental data obtained at the ISAN and by other research groups.

We demonstrate the RZLINE code capabilities with the example of simulating the key characteristics of the laser plasma produced in the interaction of the main CO_2 laser pulse with the dome-shaped target formed under picosecond prepulse irradiation. The calculated plasma emission spectrum in the 12–20 nm range and on the scale of the 13.5 ± 0.135 nm spectral band is exemplified in Fig. 6. The calculated spectrum was taken at an angle of 0° to the normal, which is assumed to coincide with the laser axis in RZLINE, the z axis pointing towards the laser system. Figure 7 depicts the spatial profile of the plasma emission intensity (the energy brightness) in projections at 0° and 90° to the normal at the instant of the peak power of laser radiation. The spatial distributions of the electron temperature and EUV radiation density corresponding to the same instant are shown in Fig. 8. The RZLINE code also permits calculating the energy spectrum of the ions (Fig. 9a) emanating from the plasma and the angular distribution of ion fluxes (Fig. 9b). These data hold significance in calculating the contamination of the collector surface by plasma streams.

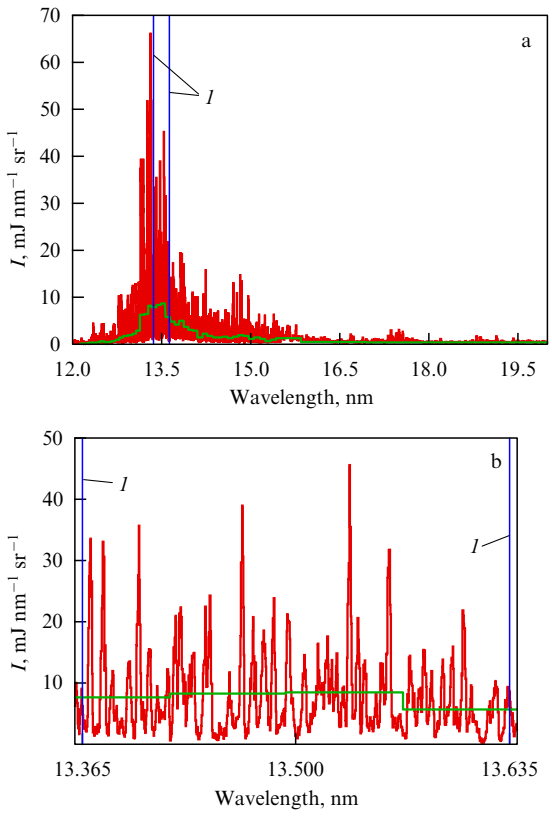

Figure 6. (Color online.) Time-integrated emission spectrum of the EUV source recorded at an angle of 0° to the normal. Blue lines (*1*) denote the limits of the 13.5 ± 0.135 nm spectral band.

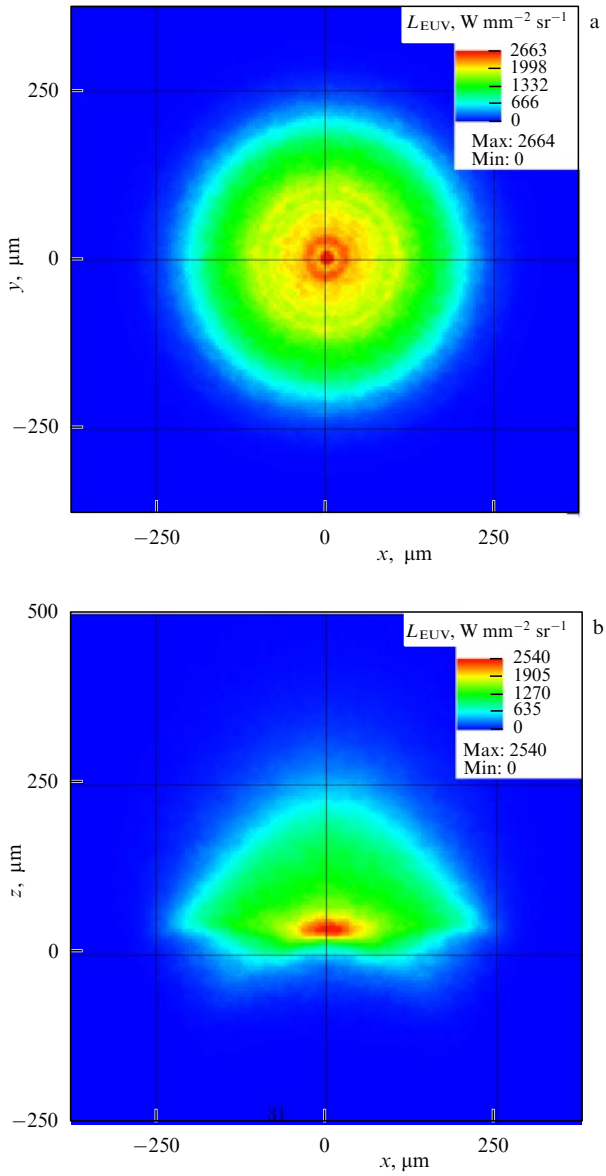

Figure 7. Energy brightness of the EUV source in the 13.5 ± 1% spectral band in projections (a) 0° and (b) 90° to the normal at the instant of peak brightness of the laser radiation.

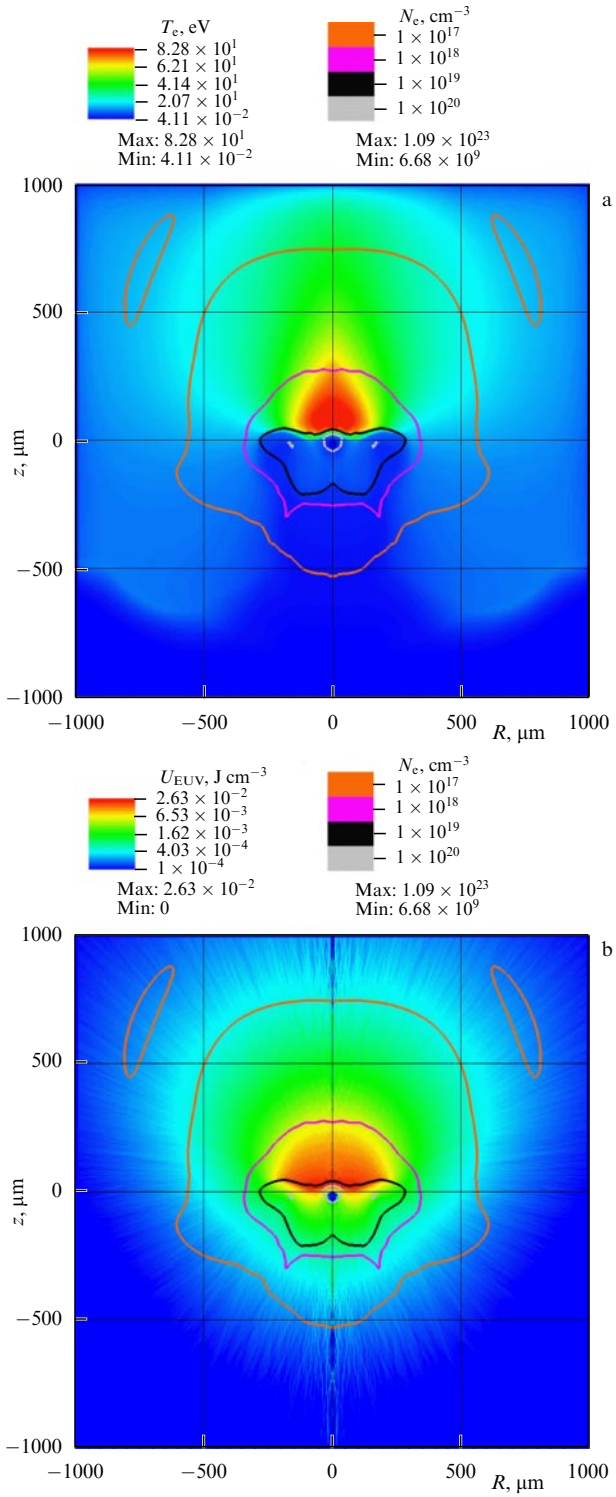

Figure 8. Spatial distributions of (a) the electron temperature and (b) the EUV radiation density in the spectral band 13.5 ± 1% nm at the instant of peak power of laser radiation. The closed contours denote the electron density N_e.

2.4 First-mirror protection

Every laser plasma burst in the EUV source chamber results in the expansion of the target substance into the full solid angle. The optimal source operation mode implies complete tin target conversion to the plasma state, and the expanding substance streams therefore consist primarily of tin ions and electrons. A significant fraction of the vaporized target mass flies towards the first mirror, the radiation collector. The contamination of the mirror surface by tin cannot be tolerated because it entails a rapid decline in its reflectivity for EUV radiation. Undisturbed source operation therefore requires an efficient protection of the first mirror from plasma streams. For this, a strong magnetic field [52–54] and protection with a buffer gas [55, 56] can be used. A sufficiently strong magnetic field can divert the trajectories of motion of the tin ions away from the first mirror surface. The gas-assisted protection implies the deceleration of tin ions in the gas medium. In this case, only those ions can be used that have a relatively high transparency at a wavelength of 13.5 nm. Among these gases are argon, helium, and hydrogen [57]. Hydrogen is the most transparent of the above gases, and therefore it is precisely this gas that is used in systems of gas-assisted protection of industrial EUV radiation sources [4, 6]. Moreover, hydrogen forms volatile SnH_x compounds with tin, which also permits using hydrogen for the removal of tin deposited on the surface of the main mirror [58].

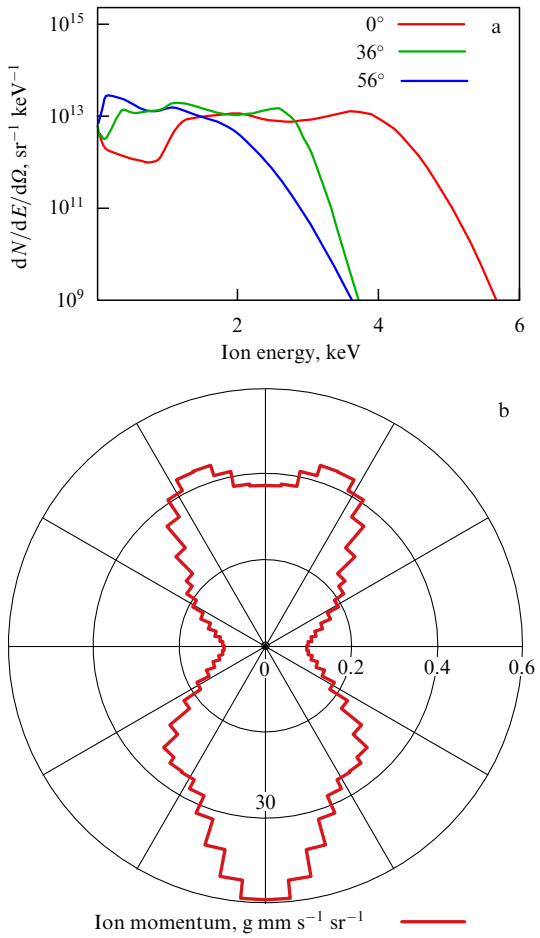

Figure 9. Energy spectrum of (a) ions emanating from the plasma and (b) the angular distribution of ion fluxes.

One of the key characteristics of gas-assisted protection is the stopping cross section σ_s for tin ions in hydrogen. For ions with a given kinetic energy E flying through a gas medium with a particle density n, σ_s is defined as

$$\sigma_s = -\frac{1}{n}\frac{dE}{dx}, \qquad (3)$$

where dE is the kinetic energy of the ion lost in its passage through a gas layer of thickness dx. At the ISAN, measurements were made of the stopping cross section for tin ions in hydrogen for the ion energy range corresponding to the operating conditions of the EUV lithography source. The measurement technique is described in Ref. [59]. Figure 10 shows the measured dependence of σ_s on E for Sn^{1+} and Sn^{2+} ions.

To investigate the efficiency of gas-assisted first-mirror protection and search for prospects to optimize it, the program code PGI [60] was developed at the ISAN. This code allows simulating the structure of gas streams in an EUV radiation source chamber. In essence, the PGI code solves gasdynamic equations for a multicomponent (H_2, H, Sn, SnH_x) gas flow with the inclusion of heat transfer, chemical reactions between individual components, and diffusion and convection of individual components.

From the standpoint of equations that describe the dynamics of a multicomponent gas flow, the laser plasma is an external quasi-point-like source of the substance of one of

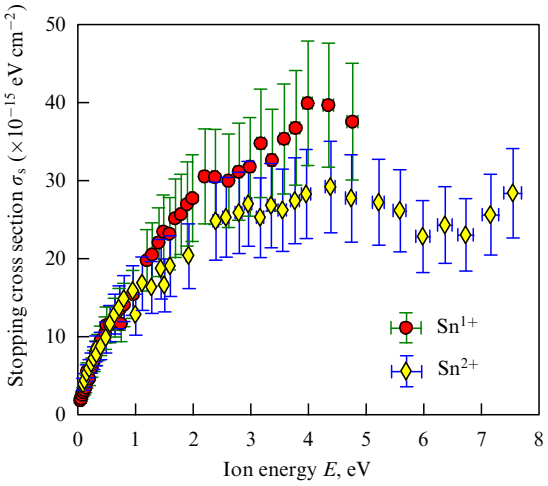

Figure 10. Dependence of the stopping cross section on the kinetic energy measured for Sn^{1+} and Sn^{2+} tin ions in hydrogen. Borrowed from Ref. [59]. © AIP Publishing. Reproduced with permission.

the flow components (Sn) as well as of energy and momentum. After every burst of the source, the tin plasma and its generated radiation expand into the full solid angle. In the course of expansion, the high-energy plasma particles (for instance, ions with the energy up to 10 keV) undergo multiple collisions with particles of the gas medium and transfer energy and momentum to them. The deceleration of the plasma streams by the gas results in some spatial distribution of the vaporized tin target mass over the chamber volume. The collisional energy transfer heats the gas that fills the source chamber.

Broadband plasma radiation is partly absorbed in the course of propagation through the gas, which also contributes to its heating. The heating and short-wavelength ($\lambda < 85$ nm) irradiation give rise to partial ionization of hydrogen. In the interaction of atomic hydrogen with the tin deposited on the chamber walls or optical surfaces, chemical reactions responsible for the formation of volatile SnH_x tin–hydrogen compounds occur [61]. The inverse reaction also occurs: the disintegration of the SnH_x molecules in their collisions with the chamber walls [61]. For a long operation of the source, a certain stationary structure of streams forms in the chamber. Against its background, diffusion and convection of the individual components of the gas phase occur. The inclusion of these processes is also of importance for the correct calculation of contaminating tin streams to the first mirror surface.

3. Sources for actinic inspection

Monitoring the state of the functional optical surface of a mask is an important element of EUV lithographic technology. The mask surface can bear defects that appear in the course of photomask production. Furthermore, the mask surface can be contaminated with time by micro- and nanoparticles. The existence of such defects and contaminants on the mask surface is intolerable because they are highly likely to give rise to critical defects in the integrated microcircuits produced by EUV microlithography. The functional mask surface must therefore undergo inspection on a regular basis.

EUV microscopy at a wavelength of 13.5 nm is the optimal tool for this task. This also requires an EUV radiation tool. Such a source must have a high average energy brightness ($B > 100$ W mm^{-2} sr^{-1}), a high stability of radiation energy dose ($3\sigma < 3.5\%$), and high spatial stability [20]. In this case, plasma sources are also highly attractive. However, mask inspection does not require a high radiation power. It is therefore possible to use collector optics with a relatively small angle of radiation collection, which is much easier to protect from the contaminating substance streams from the plasma radiation source. This greatly simplifies the task of designing a high-efficiency EUV radiation plasma source for mask inspection. For instance, in the laser plasma case, it is possible to abandon the droplet target and use a continuous renewable liquid target instead, which is much easier from the technological standpoint. Consequently, there are many more possible solutions for the construction of such a source.

Two approaches to the design of a high-brightness plasma radiation source with a wavelength of 13.5 nm were proposed at the ISAN [62]. Both approaches harness the laser plasma produced by pulsed $\lambda = 1.064$ μm Nd:YAG laser radiation. The main difference lies with the target type in use.

3.1 Tin plasma-based source

The first approach to the plasma source design involves the use of a rotating ring target of melt tin. For this purpose, a small quantity of melt tin is placed into a cylindrical vessel rotating about the vertical axis (Fig. 11). For a sufficiently fast rotation, the tin covers the inner surface of the vertical wall of the vessel and forms a liquid ring-shaped target. The laser radiation is injected and the EUV radiation is extracted at a small angle to the horizontal. Due to the fast rotation of the target, the contaminating particles (mostly the droplet fraction) escaping from the interaction zone acquire a velocity vector that rules out their arrival at the input (laser) and output (EUV) windows. Furthermore, the aperture of EUV radiation collection and the aperture of the lens that focuses the laser radiation are both limited by hollow conical structures, as shown in Fig. 11. This imposes a strong limitation on the harmful droplet, vapor, and plasma streams propagating in the direction of the optical surfaces. In addition, to suppress these harmful streams, it is planned to use a protective gas flow directed towards the plasma source and magnetic field protection.

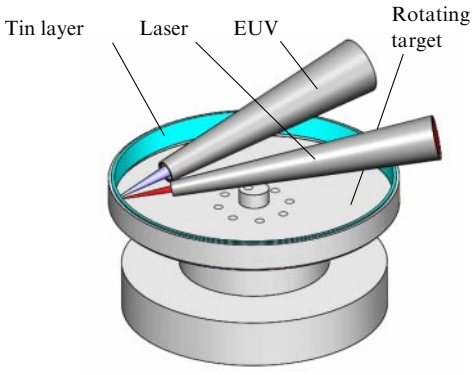

Figure 11. Schematic of an EUV radiation source that uses a rotating circular target of liquid tin for the production of laser plasma.

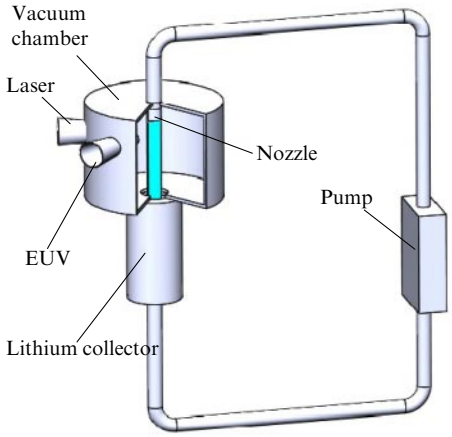

Figure 12. Schematic of an EUV radiation source that uses a liquid lithium jet target for laser plasma production.

3.2 Lithium plasma-based source

The second approach involves the use of plasma produced by pulsed laser irradiation of a liquid lithium jet target (Fig. 12). We note that the lithium plasma also permits obtaining 13.5 nm radiation by exciting the 1s–2p transition in hydrogen-like Li^{2+} ions. The efficiency of input energy conversion to the EUV radiation energy becomes lower as we pass from tin to lithium, but lithium offers several other advantages. First, the extremely narrow emission line of lithium saves us from additional spectral filtration and permits the use of Fresnel-zone plate optics. Second, lithium evaporates from optical surfaces under their heating, making it possible to design a source with self-cleaning optics. In the source, lithium circulates along a closed circuit. Its main elements are a magnetohydrodynamic pump, a conduit, and a vacuum chamber. The chamber accommodates a nozzle, which forms a jet of special configuration, and a lithium collector (see Fig. 12). The lithium jet velocity exceeds 20 m s^{-1}, which provides stable source operation for a laser pulse repetition rate of several tens of kilohertz. The design of the vacuum chamber — as well as of the input and output windows — rules out the loss of lithium due to its removal from the interaction zone.

Both approaches described above permit reaching the requisite level of 13.5 nm radiation brightness. Presently, in collaboration with the EUV Labs (Troitsk, Moscow) and ISTEQ (Netherlands) companies, the ISAN is developing prototypes of EUV radiation sources in accordance with the above approaches.

4. EUV radiation spectrometers

The investigation of short-wavelength radiation sources required the development of new spectral instruments. Recording of images with vacuum ultraviolet (VUV) microchannel plate (MCP) detectors provides frame-by-frame temporal resolution with nanosecond exposure times, which permits studying the plasma dynamics. At the ISAN, expertise in using luminescent screen–MCP assemblies for recording VUV discharge-plasma images obtained with a pinhole camera dates back to the early 1990s [63]. During the work on the EUV source, demand arose for using an MCP detector in grazing-incidence spectrometers.

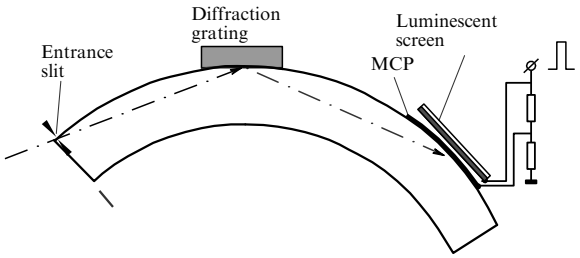

Figure 13. Schematic representation of a grazing-incidence spectrometer with an elastically bent MCP.

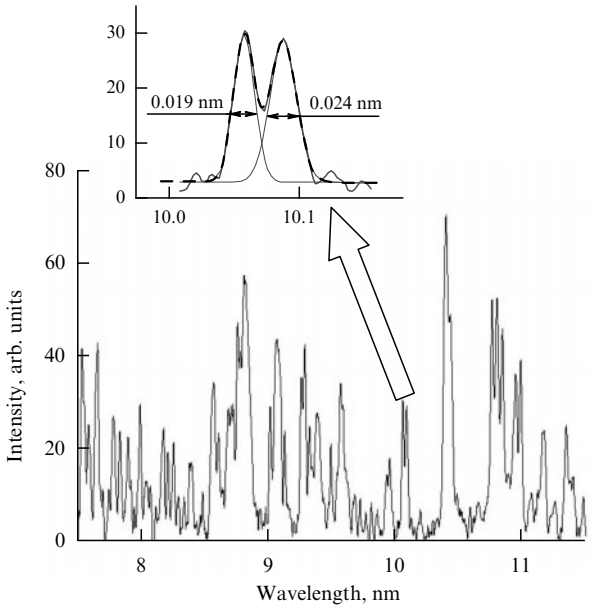

Figure 14. VUV spectrum of multiply charged Al ions in the range of 8–11 nm.

The first technological solution was the use of a classical spectrometer in combination with an MCP elastically bent along the Rowland circle [64]. The spectrometer is schematized in Fig. 13.

Although the spatial MCP resolution is not very high (50–100 μm), this spectrometer permits reaching a spectral resolving power $\lambda/\delta\lambda \sim 500$ in the 10 nm range. Figure 14 shows the spectrum of multiply charged aluminum ions in the range 8–11 nm, which demonstrates this spectral resolution. The spectrum was obtained from a low-inductance vacuum spark discharge with a peak discharge current of 100 kA.

A disadvantage of the proposed scheme is the grazing incidence of radiation on the MCP surface, which significantly lowers its sensitivity [65]. A possible solution might be to develop a flat-field spectrometer [66–68]. However, these spectrometers invite the use of a varied line-space diffraction grating, which is a rather expensive optical element.

As an alternative, implemented at the ISAN was the optical configuration of a grazing-incidence spectrometer with a conventional spherical diffraction grating, in which the entrance slit was displaced from the Rowland circle towards the grating [69]. In this configuration, the surface of spectral line focusing has a point at which the tangent to the surface is perpendicular to the line of sight (see Fig. 15). This point lies on the circumference D of a radius equal to the curvature radius of the grating G. The wavelength of the

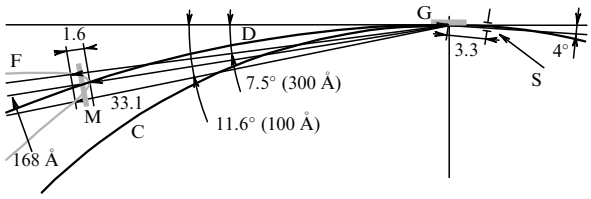

Figure 15. Diagram of a grazing-incidence spectrometer with the entrance slit displaced from the Rowland circle. Distances are indicated in cm. (Grazing angle: 40°; grating radius: 1 m; groove density: 600 mm^{-1}). S — entrance slit, G — diffraction grating, C — Rowland circle, D — circle of radius equal to the grating radius, F — surface of best spectral line focusing, M — position of the detection plane. © AIP Publishing. Reproduced with permission.

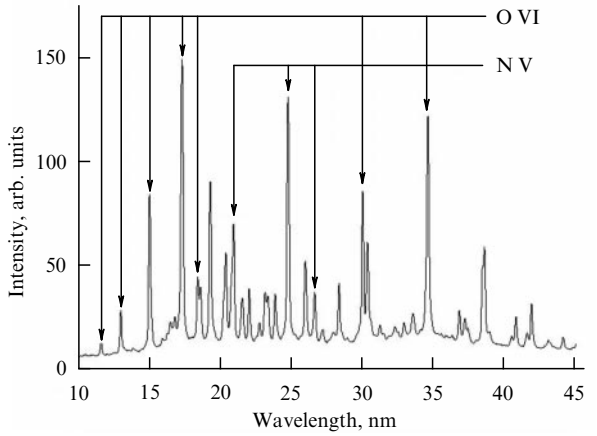

Figure 16. Capillary discharge spectrum recorded using a spectrometer with a shifted slit.

spectral line at this point is defined by the displacement of the slit from the Rowland circle [69]. The proposed optical scheme exhibits a significantly lower curvature of the focal surface than the scheme with the entrance slit placed on the Rowland circle [69]. In this scheme, it was possible to use the LPS-MCP/1F-D56 luminescent screen–MCP assembly developed at the ISAN. The calculated spectral resolving power $\lambda/\delta\lambda$ is 200–500 in the 10–40 nm range. The real attained resolving power is approximately a half of that, which is due to the low spatial resolution of the MCP. Figure 16 shows a spectrum obtained in the air capillary discharge for a peak current of 40 kA, the main lines belonging to oxygen and nitrogen. A further refinement of the proposed spectrometer implies the use of a charged-coupled device (CCD) matrix as the radiation detector, which will improve its resolving power.

5. Conclusions

We have outlined the key physical principles of the operation of a plasma radiation source intended for EUV lithography. A start on the development of an industrial radiation source based on a tin laser-produced plasma was made in 2005 [70]. In 2017, the CYMER company (a subdivision of the ASML holding company, Netherlands) demonstrated the minimal target power level (250 W) for the first time [71]. In 2018, EUV lithography facilities with a 250 W source started operating in the test mode at microcircuit manufacturers [71]. At present, the key task is to improve the ratio of the useful operation time to the downtime of the lithography facility associated with its maintenance, one of the main points of which involves

cleaning the main collector mirror of the EUV radiation source. According to estimates by Intel (USA), increasing the useful operation time by 10% corresponds to a 50 W increase in the average source power [71]. Therefore, the emphasis of development shifts from the optimization of radiating plasma parameters to the minimization of the harmful action of contaminating streams of vaporized tin on the collector mirror. At present, it may be suggested that the structure of the EUV radiation source for industrial lithography has assumed a nearly complete form.

As regards a source for actinic inspection of lithographic masks, highly diversified approaches to its construction are presently under consideration. This possibility of choice exists owing to significantly less stringent requirements imposed on this kind of radiation source, in particular, owing to the absence of the requirement of high EUV radiation power as well as to much shorter intervals of operation load. The lower output power permits abandoning the use of collector optics with large radiation collection angles, which in turn simplifies the design of the system of optics protection from contaminating substance streams inherent in plasma sources. Work on the development of high-brightness laser-plasma EUV radiation sources is underway at the ISAN. It is proposed to use continuous liquid-metal targets and solid-state lasers for the production of EUV-radiating plasma, which will make it possible to significantly simplify the source and lower the costs of its subsequent operation.

Industrial application of plasma EUV radiation sources calls for the development of compact, reliable, and simple instruments for spectral plasma diagnostics in the short-wavelength region. Several compact spectrometers have been developed at the ISAN for the diagnostics of EUV radiation sources; in particular, an optical configuration of a flat-field spectrometer has been realized without the use of costly varied line-space diffraction gratings.

Acknowledgments

This study was financially supported in part (Section 2.1) by the Russian Science Foundation (Project No. 14-11-00699). The work on the experimental investigation of the emission spectra of multiply charged tin ions was financially supported by the Russian Foundation for Basic Research (Agreement No. 16-02-00753). The tables of radiative and thermodynamic properties were calculated on the MVS-100K supercomputer.

References

1. Wagner C, Harned N *Nature Photon.* **4** 24 (2010)
2. Moors R et al. *J. Micro Nanolithogr. MEMS MOEMS* **11** 021102 (2012)
3. Hosler E R, Wood O R, in *X-Ray Lasers 2016, Proc. of the 15th Intern. Conf. on X-Ray Lasers* (Eds T Kawachi, S V Bulanov, H Daido, Y Kato) (Cham: Springer, 2018) p. 351
4. Fujimoto J et al. *J. Micro Nanolithogr. MEMS MOEMS* **11** 021111 (2012)
5. Fomenkov I V et al. *J. Micro Nanolithogr. MEMS MOEMS* **11** 021110 (2012)
6. Fomenkov I et al. *Adv. Opt. Technol.* **6** 173 (2017)
7. Jin F, Richardson M *Appl. Opt.* **34** 5750 (1995)
8. Klosner M A et al. *Opt. Lett.* **22** 34 (1997)
9. Klosner M A, Silfvast W T *Opt. Lett.* **23** 1609 (1998)
10. Koshelev K et al., in *SeMaTech EUV Source Workshop, 2002*
11. Churilov S, Ryabtsev A *Phys. Scripta* **73** 614 (2006)
12. Churilov S, Ryabtsev A *Opt. Spectrosc.* **101** 169 (2006); *Opt. Spektrosk.* **101** 181 (2006)
13. Louis E et al. *Prog. Surf. Sci.* **86** 255 (2011)
14. Banine V Y, Koshelev K N, Swinkels G H P M *J. Phys. D* **44** 253001 (2011)
15. Schriever G t al. *J. Micro Nanolithogr. MEMS MOEMS* **11** 021104 (2012)
16. Koshelev K N, Banine V E, Salashchenko N N *Phys. Usp.* **50** 741 (2007); *Usp. Fiz. Nauk* **177** 777 (2007)
17. Wagenaars E ey al. *Appl. Phys. Lett.* **92** 181501 (2008)
18. Koshelev K et al. *J. Micro Nanolithogr. MEMS MOEMS* **11** 021103 (2012)
19. Fomenkov I V et al., in *EUV Lithography* (Ed. V Bakshi) (Bellingham, WA: SPIE Press, 2018) Ch. 3A
20. Feldmann H, Ruoff J, Dinger U, in *2014 Intern. Workshop on EUV and Soft X-Ray Sources, November 3–6, 2014, Dublin, Ireland*
21. Vinokhodov A et al. *Rev. Sci. Instrum.* **87** 103304 (2016)
22. Nikiforov A F, Novikov V G, Uvarov V B *Quantum-Statistical Models of Hot Dense Matter. Methods for Computation Opacity and Equation of State* (Basel: Birkhäuser Verlag, 2005); Translated from Russian: *Kvantovo-Statisticheskie Modeli Vysokotemperaturnoi Plazmy. Metody Rascheta Rosselandovykh Probegov i Uravnenii Sostoyaniya* (Moscow: Fizmatlit, 2000)
23. THERMOS — code package and database, http://www.keldysh.ru/thermos/en
24. Novikov V G, in *Modern Methods in Collisional-Radiative Modeling of Plasmas* (Springer Series on Atomic, Optical, and Plasma Physics, Vol. 90, Ed. Yu Ralchenko) (Cham: Springer, 2016) p. 105
25. Abdallah J, Sherrill M E *High Energy Density Phys.* **4** 124 (2008)
26. Cowan R D *The Theory of Atomic Structure and Spectra* (Berkeley, CA: Univ. of California Press, 1981)
27. Gu M F *Can. J. Phys.* **86** 675 (2008)
28. Tolstikhina I et al., in *EUV Sources for Lithography* (Ed. V Bakshi) (Bellingham, WA: SPIE Press, 2006) p. 113
29. Lotz W *Z. Phys.* **206** 205 (1967)
30. Lotz W *Z. Phys.* **216** 241 (1968)
31. Lotz W *Z. Phys. A* **220** 466 (1969)
32. Lotz W *Z. Phys. A* **232** 101 (1970)
33. Regemorter H V *Astrophys. J.* **136** 906 (1962)
34. Kramers H *London Edinburgh Dublin Philos. Mag. J. Sci.* **46** 836 (1923)
35. Zhdanov V P *Sov. Phys. JETP* **48** 611 (1978); *Zh. Eksp. Teor. Fiz.* **75** 1214 (1978)
36. Basko M M *Phys. Plasmas* **23** 083114 (2016)
37. Novikov V G, Solomyannaya A D *High Temp.* **36** 835 (1998); *Teplofiz. Vys. Temp.* **36** 858 (1998)
38. Novikov V G, Zakharov S V *J. Quant. Spectrosc. Radiat. Transf.* **81** 339 (2003)
39. Novikov V G et al. *High Energy Density Phys.* **3** 198 (2007)
40. Matsukuma H et al. *Appl. Phys. Lett.* **107** 121103 (2015)
41. Vinokhodov A Yu et al. *Quantum Electron.* **46** 23 (2016); *Kvantovaya Elektron.* **46** 23 (2016)
42. Krivokorytov M S et al. *Phys. Rev. E* **95** 031101(R) (2017)
43. Basko M M et al. *Laser Phys. Lett.* **14** 036001 (2017)
44. Krivokorytov M S et al. *Sci. Rep.* **8** 597 (2018)
45. Grigoryev S Yu et al. *Phys. Rev. Applied* **10** 064009 (2018)
46. Basko M M et al. *Laser Phys. Lett.* **14** 036001 (2017)
47. Kurilovich D et al. *Phys. Rev. Appl.* **6** 014018 (2016)
48. Kurilovich D et al. *Phys. Plasmas* **25** 012709 (2018)
49. Reijers S A et al. *J. Appl. Phys.* **124** 013102 (2018)
50. O'Sullivan G, Kilbane D, D'Arcy R *J. Mod. Opt.* **59** 855 (2012)
51. Koshelev K et al. *J. Micro Nanolithogr. MEMS MOEMS* **11** 021112 (2012)
52. Harilal S S, O'Shay B, Tillack M S *J. Appl. Phys.* **98** 036102 (2005)
53. Ueno Y et al. *Appl. Phys. Lett.* **92** 211503 (2008)
54. Elg D T et al. *J. Micro Nanolithogr. MEMS MOEMS* **14** 013506 (2015)
55. Bleiner D, Lippert T *J. Appl. Phys.* **106** 123301 (2009)
56. Nakamura D et al. *J. Appl. Phys.* **102** 123310 (2007)
57. Harilal S S et al. *Appl. Phys. B* **86** 547 (2007)
58. van Herpen M M J W et al. *Chem. Phys. Lett.* **484** 197 (2010)
59. Abramenko D B et al. *Appl. Phys. Lett.* **112** 164102 (2018)
60. Astakhov D, in *2016 Intern. Workshop on EUV and Soft X-Ray Sources, November 7–9, 2016, Amsterdam, The Netherlands* (Bellingham, WA: SPIE Press, 2016)
61. Ugur D et al. *Chem. Phys. Lett.* **552** 122 (2012)

62. Antsiferov P S et al., US Patent US9476841B1 (2016)
63. Sopkin Yu V et al. *Phys. Lett. A* **152** 215 (1991)
64. Antsiferov P S et al. *Instrum. Exp. Tech.* **58** 696 (2015); *Prib. Tekh. Eksp.* (5) 121 (2015)
65. Hirata M et al. *Rev. Sci. Instrum.* **61** 2566 (1990)
66. Kita T et al. *Appl. Opt.* **22** 512 (1983)
67. Vishnyakov E A, Shatokhin A N, Ragozin E N *Quantum Electron.* **45** 371 (2015); *Kvantovaya Elektron.* **45** 371 (2015)
68. Vishnyakov E A et al. *Quantum Electron.* **46** 953 (2016); *Kvantovaya Elektron.* **46** 953 (2016)
69. Antsiferov P S, Dorokhin L A, Krainov P V *Rev. Sci. Instrum.* **87** 053106 (2016)
70. Myers D W et al. *Proc. SPIE* **5751** 248 (2005)
71. Turkot B, in *2018 EUVL Workshop, June 11 – 14, 2018, Berkeley, CA, USA*